Evolutionary adaptation of the chromodomain of the HP1-protein Rhino allows the integration of chromatin and DNA sequence signals

Lisa Baumgartner[1,2], Jonathan J. Ipsaro[3], Ulrich Hohmann[1,4], Dominik Handler[1], Alexander Schleiffer[1,4], Peter Duchek[1], Julius Brennecke[1,*]

[1] Institute of Molecular Biotechnology of the Austrian Academy of Sciences (IMBA), Vienna BioCenter (VBC), Dr. Bohr-Gasse 3, 1030 Vienna, Austria.

[2] Vienna BioCenter PhD Program, Doctoral School of the University of Vienna and Medical University of Vienna, Vienna, Austria.

[3] Howard Hughes Medical Institute, W.M. Keck Structural Biology Laboratory, Cold Spring Harbor Laboratory, 1 Bungtown Road, Cold Spring Harbor, NY 11724, United States.

[4] Research Institute of Molecular Pathology (IMP), Vienna BioCenter (VBC), 1030 Vienna, Austria.

[*] Correspondence to: julius.brennecke@imba.oeaw.ac.at

ABSTRACT

Members of the diverse heterochromatin protein 1 (HP1) family of proteins play crucial roles in heterochromatin formation and maintenance. Despite the similar affinities of their chromodomains for di- and tri-methylated histone H3 lysine 9 (H3K9me2/3), different HP1 proteins exhibit distinct chromatin binding patterns, presumably due to their interactions with various specificity factors. Here, we elucidate the molecular basis of the protein-protein interaction between the HP1 protein Rhino, a critical factor of the *Drosophila* piRNA pathway, and Kipferl, a DNA sequence-specific C_2H_2 zinc finger protein and Rhino guidance factor. Through phylogenetic analyses, structure prediction, and *in vivo* genetics, we identify a single amino acid change within Rhino's chromodomain, G31D, that does not affect H3K9me2/3 binding but abolishes the specific interaction between Rhino and Kipferl. Flies carrying the *rhino*^{G31D} mutation phenocopy *kipferl* mutant flies, with Rhino redistributing from piRNA clusters to satellite repeats, causing pronounced changes in the ovarian piRNA profile of *rhino*^{G31D} flies. Thus, Rhino's chromodomain serves as a dual-specificity module, facilitating interactions with both a histone mark and a DNA-binding protein.

INTRODUCTION

Transposable elements (TEs) are ubiquitous in eukaryotic genomes but pose a significant threat to genome integrity (Bourque et al., 2018). When activated and mobile, these selfish genetic elements can lead to insertional mutagenesis and ectopic recombination events, imposing significant fitness costs on their hosts. To counteract the deleterious effects of TEs, eukaryotes package TE loci into repressive heterochromatin, effectively silencing these elements and preventing their uncontrolled movement within the genome (Levin and Moran, 2011, Fedoroff, 2012). Proteins of the heterochromatin protein 1 (HP1) family play a central role in the initiation and maintenance of heterochromatin from fungi to animals (Vermaak and Malik, 2009).

The founding member of the HP1 family, *Drosophila* Su(var)2-5, acts as a strong suppressor of position effect variegation (James and Elgin, 1986, Eissenberg et al., 1990, Eissenberg et al., 1992). It binds to heterochromatic histone marks and facilitates transcriptional silencing and the compaction of chromatin through the recruitment of histone methyltransferases, histone deacetylases, and other repressive activities (Vermaak and Malik, 2009, Allshire and Madhani, 2018). Most animal genomes encode multiple HP1 homologs that share a common domain architecture. They contain an N-terminal chromodomain with specific affinity for di- and tri-methylated histone H3 Lysine 9 (H3K9) peptides (Bannister et al., 2001, Lachner et al., 2001), an unstructured central hinge region of variable length involved in nonspecific nucleic acid interactions (Keller et al., 2012), and a C-terminal chromo shadow domain (Aasland and Stewart, 1995). While resembling the chromodomain fold, the chromo shadow domain does not bind histone tails. Instead, it forms a dimerization interface with the chromo shadow domain of another HP1 protein, creating a binding groove for proteins containing a PxV/LxL consensus motif (Smothers and Henikoff, 2000).

The number of HP1 family members varies between species. For instance, mice and humans encode three HP1 family proteins (HP1α, HP1β, HP1γ), whereas *Drosophila melanogaster* encodes five different members: the ubiquitously expressed HP1a/Su(var)2-5, HP1b, and HP1c proteins, and the germline-specific HP1d/Rhino (ovary and testis) and HP1e (testis) proteins (Vermaak and Malik, 2009, Levine et al., 2012). Despite having similar affinities for H3K9me2/3 reported from *in vitro* experiments, the *Drosophila* HP1 proteins have distinct biological functions and chromatin-binding patterns (Yu et al., 2015, Lee et al., 2019, Baumgartner et al., 2022). For example, while Su(var)2-5 binds all H3K9-methylated loci genome-wide, the germline-specific Rhino is enriched only at specific heterochromatic loci from where the non-coding precursors of PIWI-interacting RNAs (piRNAs) are transcribed

(Vermaak et al., 2005, Klattenhoff et al., 2009, Mohn et al., 2014, Zhang et al., 2014). These so-called piRNA clusters are rich in repetitive sequences and serve as heritable sequence storage units that confer specificity to the piRNA pathway, a small RNA-based TE silencing system in animal gonads (Brennecke et al., 2007, Czech et al., 2018, Ozata et al., 2018). At the molecular level, Rhino facilitates the productive expression of heterochromatic piRNA clusters by recruiting specific effector proteins that stimulate transcription initiation, elongation, and nuclear export of the resulting non-coding piRNA precursors (Klattenhoff et al., 2009, Mohn et al., 2014, Zhang et al., 2014, Chen et al., 2016, Andersen et al., 2017, ElMaghraby et al., 2019, Kneuss et al., 2019). This makes Rhino a remarkably specialized HP1 protein that mediates activating rather than repressive chromatin identity. The tight regulation of Rhino's chromatin-binding profile is therefore of great importance.

The zinc finger protein Kipferl, one of about ninety ZAD zinc finger proteins in *Drosophila*, acts as a critical guidance factor for Rhino in ovaries (Baumgartner et al., 2022). Kipferl binds to chromatin at genomic sites enriched in GRGGN motifs, presumably through a direct interaction between its C_2H_2 zinc finger arrays and DNA. When genomic Kipferl binding sites are located within an H3K9me2/3 domain, Kipferl recruits Rhino, and both proteins form extended binding domains around initial nucleation sites. The interaction between Kipferl and Rhino occurs between Kipferl's fourth zinc finger and Rhino’s chromodomain. This interaction represents a highly unusual mode of binding because, unlike other interactions with HP1 proteins, it does not involve the dimeric HP1 chromo shadow domain.

Here, we reveal the molecular basis underlying the interaction between Kipferl and the Rhino chromodomain. We pinpointed a single amino acid adaptation within the chromodomain of Rhino that discriminates it from all other HP1 family members and that is critical for the specific Kipferl-Rhino interaction. Our findings provide important insights into how a direct protein-protein interaction governs the chromatin binding profile of an HP1 protein, illustrating how a single amino acid residue can contribute to the emergence of a novel protein function.

RESULTS

Phylogenetic and structure prediction analyses of the Rhino-Kipferl interaction

Previous yeast two-hybrid (Y2H) experiments revealed a direct interaction between Kipferl and the chromodomain of Rhino, but not with that of the related Su(var)2-5 protein (Figure 1A) (Baumgartner et al., 2022). To investigate how the binding specificity of Kipferl for Rhino is ensured, we performed a comparative phylogenetic analysis of the chromodomains of Rhino, Su(var)2-5, HP1b, HP1c and HP1e homologs from different *Drosophila* species in which Kipferl orthologs could be unambiguously identified (Figure 1B; Figure 1 – figure supplement 1, Figure 1 – figure supplement 2). In this analysis, two residues stood out as Rhino-specific and conserved sequence alterations: the D31G mutation and the G62 insertion (Figure 1B).

To determine whether either of the two Rhino-specific residues could contribute to the interaction with Kipferl, we used AlphaFold2 Multimer (Jumper et al., 2021, Evans et al., 2022) to predict interactions between Rhino's chromodomain and Kipferl's first zinc finger array, which is composed of four C_2H_2 zinc fingers and was identified as interaction site with Rhino (Baumgartner et al., 2022). AlphaFold2 Multimer predicted a high confidence interaction with a single conformation in 5/5 models between both proteins, involving the fourth zinc finger of Kipferl, which was identified as necessary and sufficient for the Y2H interaction (Figure 1C, Figure 1 – figure supplement 3A, B, C) (Baumgartner et al., 2022). No interaction was predicted between Kipferl and the Su(var)2-5, HP1b, HP1c, or HP1e chromodomains. The predicted Kipferl-Rhino complex is compatible with binding to the H3K9me2/3 peptide through Rhino's aromatic cage (Figure 1C) and would further allow for a potential dimerization of the Rhino chromodomain (Yu et al., 2015).

In the predicted complex, Kipferl's fourth zinc finger interacts with Rhino's chromodomain through an extended interface opposite of the aromatic cage, including β-sheets 2-4 and the C-terminal α-helix of the Rhino chromodomain. Centrally located in the predicted interface is the Rhino-specific glycine, G31, which occupies a position where all other HP1 proteins analyzed harbor a highly conserved aspartic acid (Figure 1B). Due to the nature of the predicted Kipferl-Rhino interaction, the exchange of glycine to aspartic acid in Rhino at position 31 would lead to steric clashes with the backbone and sidechains of Kipferl residues V285 and F286 and thus prevent the association of both proteins. We therefore hypothesized that mutating Rhino G31 to the HP1-typical aspartic acid residue ($Rhino^{G31D}$) should specifically uncouple Rhino and Kipferl while leaving Rhino otherwise intact.

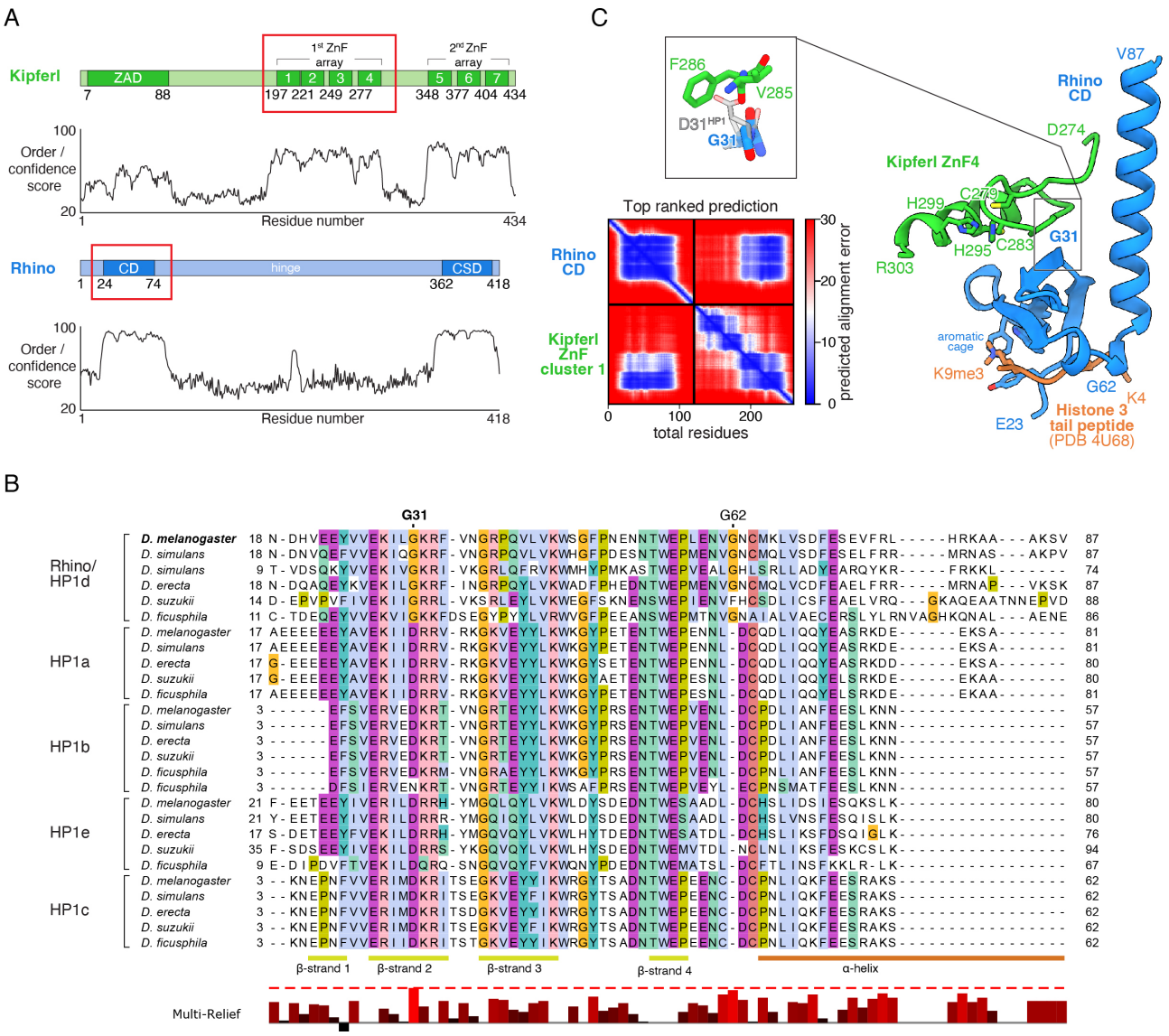

Figure 1: Structure prediction and phylogenetic analyses point to a Rhino-specific residue involved in binding Kipferl.

(A) Domain organization of Kipferl and Rhino, with the AlphaFold pLDDT score plotted as a measure of order or disorder alongside. Red boxes indicate the smallest interacting fragments identified by yeast two-hybrid experiments by Baumgartner et al. (Baumgartner et al., 2022). ZAD, Zinc finger associated domain; ZnF, Zinc finger; CD, chromodomain; CSD, chromo shadow domain **(B)** Multiple sequence alignment of HP1 family proteins in five selected species harboring an unequivocally identified Kipferl homolog (see Figure 1 – figure supplement 3). Rhino-specific amino acid residues are indicated. Protein accessions and identifiers are documented in Supplementary File 1. Multi-Relief representation indicates residues that differ significantly in Rhino homologs versus other HP1 variant proteins. **(C)** PAE plot for the top ranked AlphaFold2 Multimer prediction of the Rhino chromodomain with the Kipferl ZnF cluster 1 (left) and structure of the complex in cartoon representation (Rhino, blue; Kipferl, green), together with the H3K9me3 peptide (orange) as observed in a Rhino – H3 crystal structure (PDB ID 4U68). Key residues of Rhino's aromatic cage and H3K9me3, as well as of Kipferl's C_2H_2 ZnF4 are shown in sticks representation. Only the interacting ZnF4 is shown. Depicted in the inset are Rhino G31 and HP1 D31, with HP1 (PDB ID 6MHA) superimposed on Rhino chromodomain residues 26-57 (RMSD = 0.55 Å), together with Kipferl V285 and F286, illustrating that D31 would lead to steric clashes with Kipferl.

The Rhino^{G31D} chromodomain retains H3K9me3 binding *in vitro*

Rhino's *in vivo* function strictly depends on its ability to bind H3K9me2/3 via its chromodomain (Yu et al., 2015). In addition, it has been suggested that dimerization of the Rhino chromodomain is important for its function (Yu et al., 2015). To assess whether the Rhino G31D mutation impairs either of these functions, we analyzed a panel of recombinantly expressed Rhino chromodomains, including the wildtype construct, two putative Kipferl-binding mutants (G31A and G31D), and control mutants that impair H3K9me2/3 binding (mutations of the aromatic cage residues Y24A, W45A, or F48A) or putative dimerization (F34A/F76A double mutant) (Yu et al., 2015).

We used analytical size-exclusion chromatography with inline multi-angle light scattering (SEC-MALS) to assess the oligomeric state of the various Rhino chromodomain constructs. While our data replicated differences in elution volume between different mutant constructs (Yu et al., 2015), these did not correspond to substantial changes in their in-solution molecular weight, indicating that the oligomeric state remained the same for all constructs tested (Figure 2A; Figure 2 – figure supplement 1A). We conclude that the wildtype Rhino chromodomain, as well as the G31D or G31A variants, are monomeric in solution, as has been shown for other HP1 homologs (Jacobs et al., 2001, Brasher et al., 2000). To further test whether the G31D mutation leads to any unwanted structural changes in the Rhino chromodomain, we performed circular dichroism spectroscopy. All tested mutant constructs exhibited similar secondary structure composition compared to the wildtype construct (Figure 2 – figure supplement 1B).

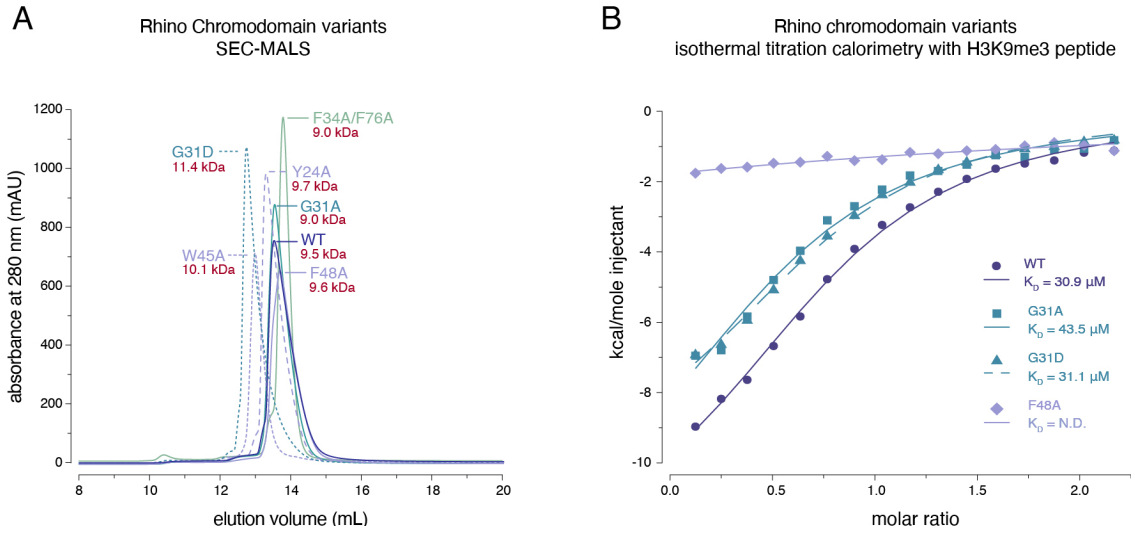

Figure 2: G31 point mutations do not affect Rhino's ability to bind H3K9me3.
(A) Line graph summarizing SEC-MALS results for the examined Rhino chromodomain constructs. The in solution molecular weight is indicated for each construct. **(B)** Isothermal titration calorimetry results showing the binding of indicated Rhino chromodomain constructs to the H3K9me3-modified histone tail peptide.

Having established that the two G31 mutant chromodomains do not exhibit altered protein folding or oligomeric state, we tested both constructs for their ability to bind H3K9me3 peptides alongside wildtype and aromatic cage mutant (F48A) controls. Consistent with previous observations (Yu et al., 2015, Le Thomas et al., 2014), isothermal titration calorimetry (ITC) experiments using synthetic H3K9me3 peptides revealed an affinity of 30.9 ± 3.0 μM for the wildtype domain and no measurable affinity for the F48A mutant (Figure 2B). Despite slight changes in the thermodynamic binding parameters, both the G31A and G31D mutants showed affinities comparable to the wildtype constructs with 43.5 ± 8.6 μM and 31.1 ± 3.2 μM, respectively. Thus, the Rhino^{G31D} chromodomain behaves similarly to the wildtype construct in terms of oligomeric state, folding, and ability to bind H3K9me3 peptides *in vitro*.

The *rhino^{G31D}* mutant uncouples Rhino from Kipferl

To investigate the importance of G31 for Rhino function *in vivo*, we introduced a single point mutation into the endogenous *rhino* locus, reverting G31 to the aspartic acid found in all other HP1 proteins (*rhino^{G31D}*). In *kipferl* mutant females, Rhino fails to localize to most of its genomic binding sites, resulting in reduced piRNA levels and impaired fertility (Baumgartner et al., 2022). Females homozygous for the *rhino^{G31D}* allele were viable but exhibited severely reduced fertility: while the egg-laying rate of *rhino^{G31D}* females was comparable to that of control flies, the hatching rate of laid eggs dropped to 21 ± 9 % (Figure 3A). This decrease in fertility was less severe than the complete sterility seen for *rhino* null mutants, but similar to that observed in *kipferl* null mutants (Baumgartner et al., 2022), providing a first indication that the G31D mutation may specifically affect the Rhino–Kipferl interaction.

To gain more direct insight into the Rhino–Kipferl interaction in *rhino^{G31D}* mutants, we examined changes in the typically pronounced colocalization of Kipferl and Rhino at discrete nuclear foci—corresponding to piRNA source loci—that is seen in wild-type nurse cells (Baumgartner et al., 2022). Using immunofluorescence imaging, we found a complete lack of colocalization of Rhino and Kipferl in *rhino^{G31D}* ovaries (Figure 3B). Kipferl localized diffusely in the nucleus with only a few foci, mirroring the localization of Kipferl in *rhino* null mutants. Rhino^{G31D} was not enriched in these Kipferl foci, but instead accumulated in prominent structures at the nuclear envelope, reminiscent of Rhino accumulations found in *kipferl* null mutants (Baumgartner et al., 2022).

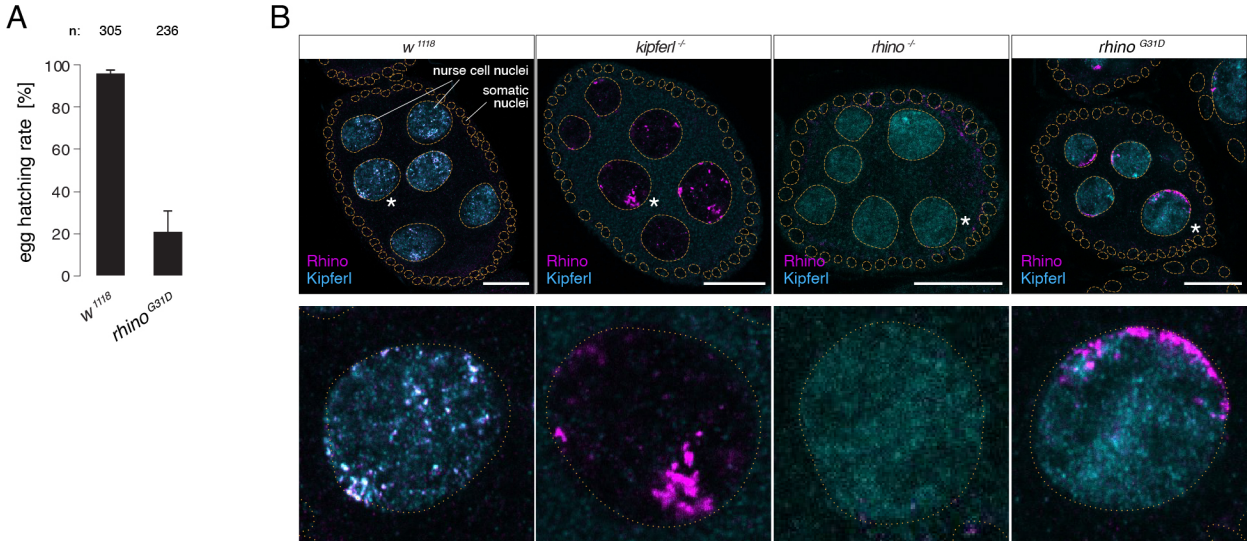

Figure 3: The *rhino*^{G31D} point mutation recapitulates the mutant phenotypes observed for Rhino and Kipferl in each other's null mutant background.
(A) Bar graph depicting female fertility as egg hatching rate in percent of laid eggs for indicated genotypes. **(B)** Confocal images showing immunofluorescence signal for Kipferl and Rhino in egg chambers of indicated genotypes. Zoomed images display one representative nurse cell nucleus (labeled by white asterisk in panel A) per genotype (scale bar: 20 µm).

To determine the chromatin binding patterns of Rhino and Kipferl in ovaries of *rhino*^{G31D} mutant flies, we performed chromatin immunoprecipitation followed by sequencing (ChIP-seq). In wild-type ovaries, Rhino and Kipferl co-occupy hundreds of heterochromatic domains of different sizes in nearly identical enrichment patterns (Figure 4A) (Baumgartner et al., 2022). In addition, Kipferl, but not Rhino, binds to specific sites in euchromatin (Kipferl-only sites) that lack H3K9me2/3 marks but are enriched in GRGGN motifs, the presumed binding sequence of Kipferl. To account for the heterogeneous size of genomic Rhino/Kipferl domains, we analyzed their binding profiles by quantifying genome-unique ChIP-seq reads mapped to non-overlapping genomic 1 kilobase tiles (Mohn et al., 2014). In *kipferl* mutants, Rhino is lost from most of its genomic binding sites, with the tiles that retain Rhino binding primarily corresponding to piRNA clusters *38C* and *42AB* (Figure 4A, B) (Baumgartner et al., 2022). Conversely, in *rhino* mutants, Kipferl binding is still detected at euchromatic Kipferl-only sites, but it is strongly reduced at loci that are co-occupied by Kipferl and Rhino in wildtype: at sites where Rhino binding is Kipferl-dependent, Kipferl binding is reduced to more defined, narrow peaks. At Kipferl-independent loci on the other hand (e.g., piRNA clusters *38C* and *42AB*), Kipferl binding is almost completely lost in *rhino* mutants (Figure 4A). ChIP-seq experiments in *rhino*^{G31D} mutant ovaries revealed a chromatin occupancy for Rhino^{G31D} that was almost indistinguishable from that of wild-type Rhino in *kipferl* mutants (Figure 4C, D). This extended to Kipferl-independent loci (e.g., piRNA clusters *38C* and *42AB*),

where the slightly altered chromatin occupancy of Rhino in *kipferl* mutants was mirrored by Rhino^{G31D} (Figure 4A). At the same time, the chromatin binding profile of Kipferl in *rhino^{G31D}* mutants strongly resembled that seen in *rhino* null-mutants genome-wide (Figure 4A, E). Taken together, mutation of a single Rhino-specific chromodomain residue to its ancestral state leads to the functional uncoupling of Rhino and Kipferl at the molecular level.

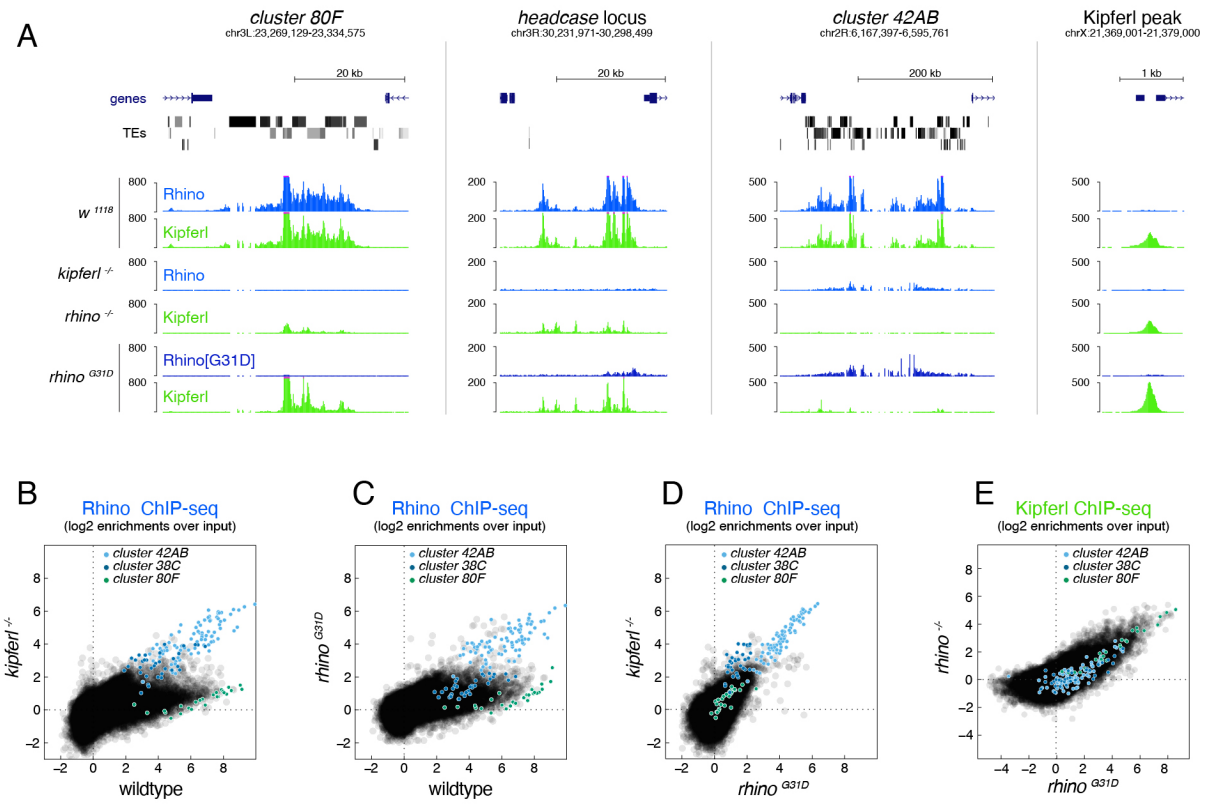

Figure 4: The Rhino^{G31D} point mutation uncouples Rhino and Kipferl at chromatin.
(A) UCSC genome browser screenshots depicting the ChIP-seq signal for Rhino and Kipferl at diverse Rhino domains in ovaries of the indicated genotypes (signal shown as coverage per million sequenced reads for one representative replicate). **(B-E)** Scatter plot of genomic 1-kb tiles contrasting average log2-fold ChIP-seq enrichment for Rhino (B-D) or Kipferl (E) in ovaries of the indicated genotypes (values displayed represent the average of two to three replicate experiments)

Rhino^{G31D} is functional at Kipferl-independent piRNA source loci

To determine whether the Rhino^{G31D} point mutation affects the overall function of Rhino, we analyzed Kipferl-independent piRNA source loci. In *kipferl* mutant ovaries, Rhino is sequestered to large DNA satellite arrays, leading to greatly increased transcription and piRNA production at the *Responder* and

1.688 g/cm3 family satellites (Baumgartner et al., 2022). In *rhino*^{G31D} mutants, RNA fluorescent in situ hybridization (FISH) experiments showed that transcription of the *Rsp* and *1.688 g/cm3* satellites was also strongly elevated, resulting in elongated structures at the nuclear envelope, reminiscent of their phenotype observed in *kipferl* mutant nurse cell nuclei (Figure 5A). Consistent with their elevated transcription, Rhino^{G31D} was enriched at satellite consensus sequences as determined by ChIP-seq, while it was reduced at most transposon sequences (Figure 5B, C). These observations extended to piRNA levels: piRNAs originating from *Rsp* and *1.688 g/cm3* satellites were strongly increased (Figure 5D), while piRNAs mapping to Rhino-dependent piRNA clusters were reduced specifically at Kipferl-dependent piRNA *cluster 80F*, but not at the Kipferl-independent piRNA clusters *38C* and *42AB* (Figure 5E). This further confirmed that the Rhino^{G31D} mutation precisely phenocopies a *kipferl* null-mutant, indicating that Rhino^{G31D} is fully functional at its remaining Kipferl-independent loci.

Rhino also specifies dual-strand piRNA source loci in the male germline, where Kipferl is not expressed (Chen et al., 2021, Chen and Aravin, 2023, Baumgartner et al., 2022). piRNA source loci in testes only partially overlap with those of ovaries and are dynamically regulated during spermatogenesis. This implies Kipferl-independent mechanisms for Rhino recruitment to chromatin. To assess a potential impact of the G31D mutation on Rhino function in males, we sequenced small RNAs from testes issected from a panel of different genetic mutants. When *rhino* mutant testes were compared to wildtype controls, piRNA production from dual-strand piRNA source loci was impaired. In contrast, piRNA levels from the same loci remained essentially unchanged in *kipferl* or *rhino*^{G31D} mutants (Figure 5F). The same was observed for piRNAs derived from *Rsp* and *1.688 g/cm3* satellites, which are transcribed in a Rhino-dependent manner also in testes (Figure 5G). Taken together, the G31D mutation, while completely uncoupling Rhino from Kipferl, does not interfere with Rhino function at Kipferl-independent sites in ovaries and testes.

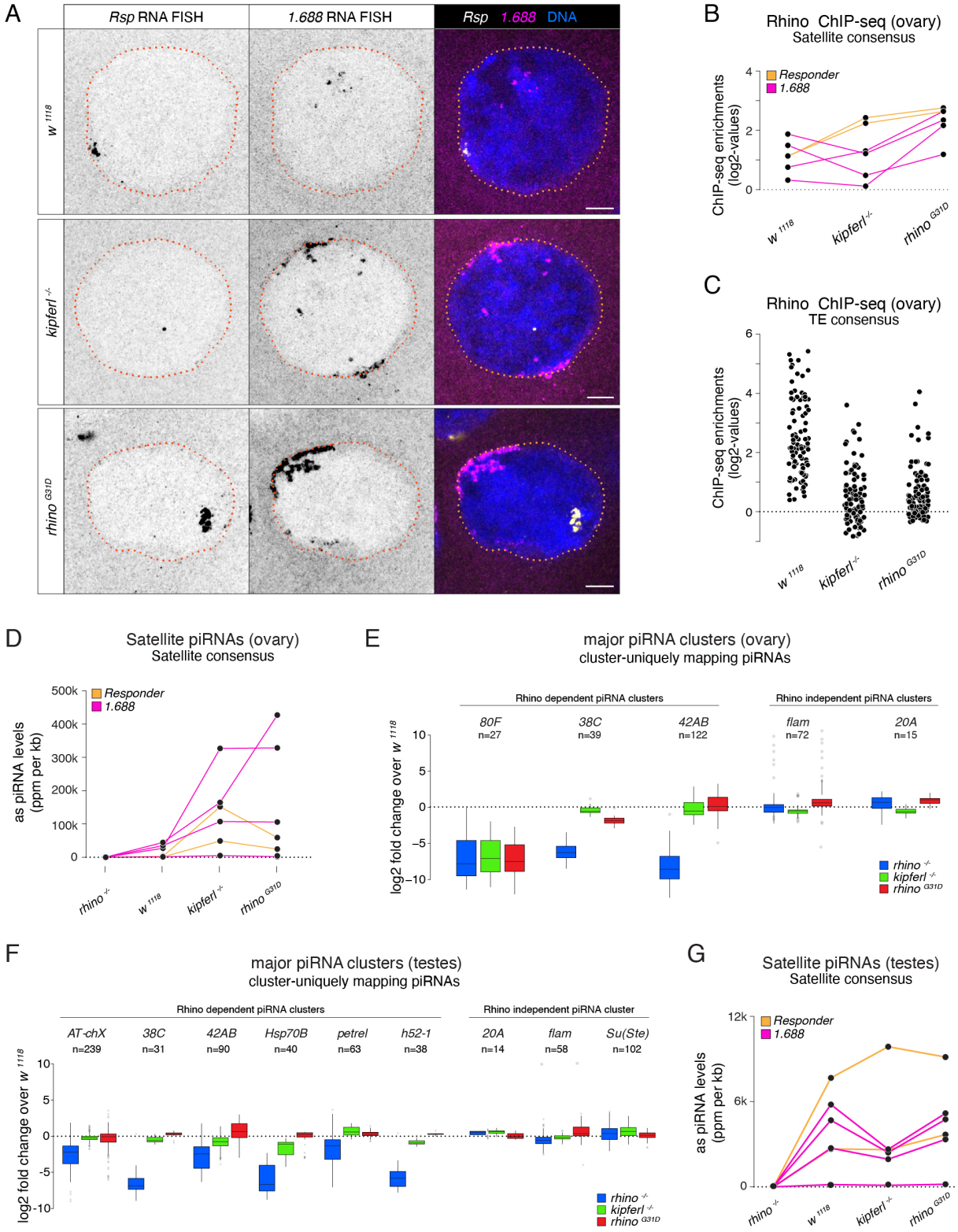

Figure 5: Kipferl-independent functions of Rhino are not affected by the G31D point mutation.
(A) Confocal images showing *Rsp* and 1.*688 g/cm3* Satellite RNA FISH signal in nurse cells of indicated genotypes (scale bar: 5 µm). **(B, C)** Jitter plots depicting the log2-fold enrichments for Rhino ChIP-seq on consensus sequences of Satellites (B) or Rhino-dependent transposons (C) in ovaries with indicated genetic

backgrounds. **(D, G)** Jitter plots depicting the length-normalized antisense piRNA counts on Satellite consensus sequences derived from ovaries (D) or testes (G) of indicated genetic backgrounds. **(E, F)** Box plots depicting the log2 fold change of piRNA counts (compared to w^{1118} control) per 1kb tile for major piRNA clusters in ovaries (E) or testes (F) of the indicated genotypes. The number of tiles per piRNA cluster is indicated as n.

CONCLUSION

In this study we show how the DNA sequence-specific zinc finger protein, Kipferl, specifically binds the chromodomain of the HP1 variant Rhino, thereby dictating Rhino's chromatin-binding profile and piRNA production in *Drosophila*. Our collective data show that reverting a single amino acid within Rhino's chromodomain to its ancestral state, G31D, abolishes Kipferl's ability to target Rhino to chromatin. Notably, the G31 residue in Rhino proteins is highly conserved among *Drosophilids*, even in species that lack a clearly identifiable Kipferl ortholog. This may indicate that other proteins use a mechanism similar to Kipferl to define Rhino's chromatin occupancy in more distantly related *Drosophila* species. Our data also show that the Rhino^{G31D} mutation does not affect the chromatin binding of Rhino at Kipferl-independent piRNA source loci in ovaries and testes, suggesting the existence of other, G31-independent recruitment mechanisms for Rhino to chromatin. Whether these alternative mechanisms act in a similar way to the one described here, utilizing zinc finger proteins and interactions with the Rhino chromodomain, remains to be determined. An important issue for future investigations, which is currently hampered by challenges in obtaining soluble recombinant Kipferl protein, will be to determine the precise three-dimensional arrangement of the Kipferl-Rhino complex together with Kipferl motif-containing DNA and H3K9-methylated nucleosomes, taking into account that Kipferl forms homodimers via its N-terminal ZAD domain and Rhino via its C-terminal chromo shadow domain.

ACKNOWLEDGMENTS

We thank the NGS, and VDRC units at VBCF, the IMBA/IMP/GMI BioOptics facility and the IMBA Fly House for their invaluable support. Circular Dichroism spectrophotometry was conducted at the Precision Biomolecular Characterization Facility (PBCF) at Columbia University, supported by NIH award 1S10OD025102-01. We thank Leemor Joshua-Tor for instrument support, Clemens Plaschka for experimental advice, and the Brennecke and Joshua-Tor laboratories for help throughout the project.

FUNDUNG STATEMENT

This research was funded by the Austrian Academy of Sciences, the European Research Council (ERC-2015-CoG-682181 to JB), the Austrian Science Fund (W1207 to JB). Circular Dichroism spectrophotometry was conducted at the Precision Biomolecular Characterization Facility (PBCF) at Columbia University, supported by NIH award 1S10OD025102-01. LB was funded by a Boehringer Ingelheim Fond PhD Fellowship, JJI was supported by funding from the Howard Hughes Medical Institute, UH was supported through the European Union's Framework Programme for Research and Innovation Horizon 2020 (Marie Curie Skłodowska grant 896416) and through an EMBO long-term fellowship (ALTF_1175-2019).

DATA AND MATERIAL AVAILABILITY

Sequencing data sets have been deposited to the NCBI GEO archive (GSE244196). Previously published data sets analyzed in this study are listed in Supplementary File 2. All fly strains generated for this study are available via the VDRC (http://stockcenter.vdrc.at/control/main).

DECLARATION OF INTERESTS

The authors declare no competing interests.

SUPPLEMENTARY FILES

Supplementary File 1

Supplementary File 2

Figure 1-figure supplement 1

Figure 1-figure supplement 2

Figure 1-figure supplement 3

Figure 2-figure supplement 1

Key Resource Table

Materials & METHODS

Fly strains and husbandry

All fly stocks were maintained at 25°C with 12h dark/light cycles. Fly strains used in this study are listed in the Key Resource Table. For ovary dissections, flies were aged for 2–6 days and held in cages with apple juice plates and fresh yeast paste for two days. Flies harboring the *rhino*^{G31D} point mutation were generated in isogenised *w*^{1118} embryos by co-injecting the pDCC6b plasmid (Gokcezade et al., 2014) expressing a gRNA (TATGTAGTGGAGAAAATCTT) with an HDR donor oligo (GGTCGATGCACCGCCTAAtGATCATGTCGAAGAATATGTAGTGGAGAAAATCcTgGatAAAC GGTTTGTTAATGGGCGTCCCCAGGTTCTGGTGAAGTGGAGCGGTTTTCCG; IDT).

Phylogenetic analyses

Kipferl and related zinc finger associated domain-containing (zf-AD) proteins were collected with NCBI BLAST searches using *Drosophila melanogaster* Kipferl zf-AD (region 5-95) in the NCBI non-redundant protein or the UniProt reference proteomes databases (Altschul et al., 1997, UniProt, 2021, Coordinators, 2018) applying significant E-value thresholds (1e^{-5}). Selected proteins, covering the zf-AD over the complete length, were aligned with MAFFT (v7.505, -linsi method) (Katoh and Toh, 2008), and the zf-AD region extracted with Jalview (Waterhouse et al., 2009). A maximum likelihood phylogenetic tree was calculated with IQ-TREE 2 (v.2.2.0) (Minh et al., 2020), with standard model selection using ModelFinder (Kalyaanamoorthy et al., 2017) and ultrafast bootstrap (UFBoot2) support values (Hoang et al., 2018). The tree was visualized in iTOL (v6) (Letunic and Bork, 2021). Branches that are supported by an ultrafast bootstrap (UFBoot) value ≥95% are indicated by a grey dot. Branch lengths represent the inferred number of amino acid substitutions per site, and branch labels are composed of gene name (if available), genus, species, and accession number. A similar approach was performed to collect Rhino and HP1 sequences. Full length D. melanogaster HP1-like sequences were used as query for blast searches applying highly significant E-value thresholds (1e-10). Only sequences covering both chromodomain (CD) and chromo shadow domain (CSD) were considered for further analysis. The alignment was condensed by removing all columns covering less than 70% of the sequences and a maximum likelihood phylogenetic tree was inferred. To search for residues in Rhino that are distinct from all other HP1-like families, we focused on 17 *Drosophila* species where Kipferl could be detected and extracted 104 protein sequences. In the resulting alignment, sub-family specific residues were detected with the multi-relief method (https://www.ibi.vu.nl/programs/shmrwww/) (Brandt et al., 2010).

AlphaFold predictions

AlphaFold2-Multimer (Jumper et al. 2021, Evans et al. 2021) was used to predict protein-protein interactions on a local GPU cluster with a script using MMseqs2 (Steinegger and Soding, 2017) (git@92deb92) for local MSA creation and Colabfold (Mirdita et al., 2022) (git@7227d4c) for structure prediction. Protein structures were analyzed using ChimeraX (Pettersen et al., 2021).

Expression and purification of the Rhino chromodomain

His_6-SUMO-RhinoCD constructs (spanning Rhino residues 20-90 in the vector pET-28) were transformed into the *E.coli* strain BL21-CodonPlus (DE3)-RIPL (Agilent) for large-scale expression using standard methods. Briefly, cultures were grown in Terrific Broth media supplemented with appropriate antibiotic(s) at 37°C to a culture density of approximately $OD_{\lambda=600\ nm}$ of 1.2. Cultures were then cooled in an ice water bath for 15 minutes followed by induction of protein expression with 0.5 mM IPTG. Induction proceeded overnight at 16°C with shaking at 220 rpm. Cells were harvested by centrifugation at 4000*g* for 30 minutes at 4°C. For Ni-NTA purification, cell pellets were resuspended in 20 mL lysis buffer (50 mM sodium phosphate, pH 8.0, 50 mM NaCl, 10 mM imidazole, 10 µg/mL DNase I, and protease inhibitors) per liter culture. The resuspended cells were lysed by sonication and the lysate was then clarified by ultracentrifugation at roughly 140,000*g* for 30 minutes. The soluble supernatant was taken for affinity purification via Ni-NTA column (1.5 mL of beads per liter culture), pre-equilibrated with lysis buffer. Beads were washed with 10 column volumes of wash buffer (50 mM sodium phosphate, pH 8.0, 200 mM NaCl, 10 mM imidazole) followed by elution of the target protein in 50 mM sodium phosphate, pH 8.0, 100 mM NaCl, 150 mM imidazole. To remove the affinity tag, Ulp1 protease was added in a 1:10 mass ratio (protease:RhinoCD) and incubated overnight at 4°C. 1 mM EDTA and 5 mM DTT (final concentrations) were added to limit degradation and enhance tag cleavage, respectively. The protein was further purified using tandem ion exchange chromatography with HiTrap Q HP and HiTrap SP HP columns (Cytiva/GE Healthcare Life Sciences). Digested protein was first diluted three-fold with low salt buffer (20 mM Tris, pH 7.5, 1 mM DTT) then applied to the HiTrap Q column. The flowthrough was collected and purified using the HiTrap SP column. The target protein was eluted using a 0-1 M NaCl gradient in 20 mM Tris, pH 7.5, and 1 mM DTT over approximately 60 mL. Peak fractions were assessed by SDS-PAGE then selected and pooled for further purification. Pooled fractions were concentrated and further purified by gel filtration chromatography using a Superdex75 column equilibrated with 20 mM Tris, pH 7.5, 150 mM NaCl, 1 mM DTT. Depending on the total yield, either a Superdex75increase 10/300 column or a Superdex75 HiLoad 16/600 column (Cytiva/GE Healthcare Life Sciences) was used. Peak fractions were assessed by SDS-PAGE. Fractions with highly

purified protein were concentrated, then stored at 4°C. For long-term storage the protein was flash frozen in liquid nitrogen then kept at -80°C. Typical yields were 1-10 mg of purified protein (>98% pure as assessed by SDS-PAGE) per liter culture.

Size exclusion chromatography with inline multiangle light scattering (SEC-MALS)

Multiangle light scattering was used to determine the oligomeric state of the purified proteins. Roughly 400 µg of purified protein (100 µL at 4 mg/mL) was taken for in-line size exclusion chromatography on a Superdex75increase 10/300 GL column (monitored at 280 nm) followed by light scattering analysis. Chromatography was performed in a buffer of 20 mM Tris, pH 7.5, 150 mM NaCl. MALS was measured with a Wyatt Dawn Heleos-II and processed using the included software (ASTRA Version 5.3.4). Bovine Serum Albumin (BSA) was used as calibration control.

Circular dichroism

Circular dichroism was used to assess the folding of the various Rhino chromodomain constructs. Prior to data collection, proteins were exchanged into 10 mM sodium phosphate, pH 7.5, 0.15 M NaF using Zeba 7 kDa spin desalting columns (ThermoFisher Scientific) then diluted to approximately 50 µM in the desalting buffer. Samples were measured in a 0.2 mm path length demountable quartz cuvette (Hellma) and data were acquired using a Chirascan V100 Spectrometer (Precision Biomolecular Characterization Facility, Columbia University). Spectra were collected at 22°C with a data pitch of 1 nm and scan speed of 1 nm/s. Data shown are the average of three scans after buffer subtraction and presented in units of mean residue ellipticity (degrees·cm^2·$dmol^{-1}$·$residue^{-1}$). Fitting was performed by DichroWeb (Miles et al., 2022) using the CONTIN-LL method (Provencher and Glockner, 1981) with reference set 3. All fits had an NRMSD of 0.1 or less.

Isothermal Titration Calorimetry (ITC)

Approximately 500 µL of each construct was dialyzed (3.5 kDa molecular weight cutoff) into 20 mM Tris, pH 8.0, 25 mM NaCl, and 2 mM βME overnight at 4°C. The protein concentration was then determined by absorbance at 280 nm after which the protein was diluted to 100 µM in dialysis buffer. H3K9me3 peptide (KQTAR-K[me3]-STGGK) was purchased from AnaSpec, Inc. and resuspended at approximately 1 mM in dialysis buffer. Calorimetry was conducted using a MicroCal iTC200 at 20°C with stirring at 750 rpm with a reference power of 11 µcal/sec. Sixteen 2.5 µL injections were performed with an injection spacing of 120 seconds. Binding curves were analyzed using the included Origin 7 SR4 (version 7.0552 (B552)) software.

398 **RNA Fluorescence In Situ Hybridization**

399 RNA FISH for *Rsp* and *1.688 g/cm3* Satellites was performed using an in-house labelled probe set
400 composed of 48 oligos or a single fluorescent oligo, respectively (Wei et al., 2021, Gaspar et al., 2017).
401 Briefly, 5 pairs of ovaries were dissected into ice-cold PBS, fixed at room temperature for 20 min (4%
402 formaldehyde, 0.3% Triton X-100 in PBS), washed 3 times for 5 min at RT (PBS containing 0.3% Triton
403 X-100) followed by incubation at 4°C overnight in 70% EtOH for full permeabilization. Ovaries were
404 rehydrated for 5 min in wash buffer (10% formamide in 2x SSC) prior to hybridization, which was done
405 in 50 µL hybridization buffer (100 mg/mL dextran sulfate and 10% formamide in 2x SSC) overnight at
406 37°C using 0.5 µL *Rsp* FISH probe per sample and a final concentration of 100 nM for the *1.688 g/cm3*
407 FISH oligo. Samples were rinsed twice in wash buffer and washed in wash buffer twice for 30 min at
408 37°C. Ovaries were counterstained for DNA (DAPI 1:5000 in 2x SSC) for 5 min at RT followed by 2
409 washes for 5 min with 2x SSC. Ovaries were mounted on microscopy slides using DAKO mounting
410 medium (Agilent) and equalized at RT for at least 24 h before imaging on a Zeiss LSM 880 inverted
411 Airyscan microscope. Images are shown as Z-stack across a maximum of 2 µm.

412

413 **Immunofluorescence staining of ovaries**

414 5-10 ovary pairs were dissected into ice cold PBS before fixation (4% formaldehyde, 0.3% Triton X-
415 100, 1x PBS) for 20 min at room temperature with rotation. Fixed ovaries were washed 3 times for 5 min
416 each in PBX (0.3% Triton X-100, 1x PBS) and blocked with BBX (0.1% BSA, 0.3% Triton X-100, 1x
417 PBS) for 30 min at room temperature with rotation. Incubation with primary antibody was performed at
418 4°C overnight with antibodies diluted in BBX. After three 5-min washes in PBX, ovaries were incubated
419 overnight at 4°C with fluorophore-coupled secondary antibodies, washed three times in PBX with DAPI
420 in the first wash (1:50,000 dilution). The final wash buffer was carefully removed before addition of
421 DAKO mounting medium. The samples were imaged on a Zeiss LSM 880 confocal-microscope and
422 image processing was done using FIJI/ImageJ (Schindelin et al., 2012). Images are shown as Z-stack
423 projection across a maximum of 2 µm. All relevant antibodies and dilutions are listed in the Key Resource
424 Table.

425

426 **Scoring of embryo hatching rates**

427 To determine female fertility, 10 females were collected as virgins, aged for 2-3 days and mated for at
428 least 24 hours with three w^{1118} males. The hatching rate of eggs laid on apple juice plates within 4-7 hours
429 was determined 30 h after collection (25°C) as the percentage of hatched eggs out of the total. Only plates
430 with more than 50 eggs were included in the analysis. Wild type females were included as a control.

431

432 **Definition and curation of 1 kb genomic windows**

433 Non-overlapping 1-kb tiles were generated based on the four assembled chromosomes of the *Drosophila*
434 *melanogaster* genome (dm6 assembly) and intersected with genomic piRNA cluster coordinates for
435 annotation. Tiles with a mappability of less than 25%, as determined by intersection with genomic blocks
436 of continuous mappability using BEDTools coverage, were excluded from all analyses (2,761 1-kb tiles).
437 In addition, tiles with more than a threefold deviation from the median values for representative input
438 libraries used in (Baumgartner et al., 2022) (18,268 1-kb tiles) or tiles with strong residual Rhino or
439 Kipferl signal in ChIP-seq libraries prepared from the respective knockout ovaries (20 and 495 tiles,
440 respectively) were removed.

441

442 **ChIP-Seq**

443 ChIP was performed as described previously (Lee et al., 2006). In brief, 150 µL of ovaries were dissected
444 into ice-cold PBS, followed by crosslinking with 1.8% formaldehyde in PBS for 10 min at room
445 temperature, quenching with glycine, and rinsing with PBS. Samples were flash frozen in liquid nitrogen
446 after removing all PBS. Frozen ovaries were disrupted in PBS using a Dounce homogenizer (tight) and
447 centrifuged at low speed. The pellet was resuspended in lysis buffer. Samples were sonicated (Bioruptor)
448 to obtain DNA fragment sizes of 200-800 bp. Samples were incubated with specific antibodies overnight
449 at 4°C in 350–700 µL total volume using 1/4 to 1/3 of chromatin per ChIP (antibodies are listed in Key
450 Resource Table). 40 µL Dynabeads (equal mixture of Protein G and A, Invitrogen) were then added and
451 incubated for 1 h at 4°C for immunoprecipitation. Following multiple washes, immunoprecipitated
452 protein-DNA complexes were eluted with 1% SDS. Treatment with RNAse-A, decrosslinking overnight
453 at 65°C, and proteinase K treatment were performed before clean-up using ChIP DNA Clean &
454 Concentrator columns (Zymo Research). Barcoded libraries were prepared using the NEBNext Ultra II
455 DNA Library Prep Kit for Illumina (NEB) according to manufacturer's instructions and sequenced on a
456 NovaSeqSP instrument (Illumina).

457

458 **Small RNA-Seq**

459 Small RNA cloning was performed as described in (Grentzinger et al., 2020). In brief, ovaries or testes
460 were lysed and Argonaute-sRNA complexes were isolated using TraPR ion exchange spin columns.
461 sRNAs were subsequently purified using acidic phenol. 3′ adaptors containing 6 random nucleotides plus
462 a 5 nt barcode on their 5′ end and 5′ adaptors containing 4 random nucleotides at their 3′ end were

subsequently ligated to the small RNAs before reverse transcription, PCR amplification, and sequencing on an Illumina NovaSeqSP instrument.

Computational Analysis

ChIP-Seq Analysis: ChIP-seq reads were trimmed to remove the adaptor sequences. Reads were mapped to the dm6 genome using Bowtie (version.1.3.0, settings: -f -v 3 -a --best --strata --sam), allowing up to three mismatches. Genome unique reads were mapped to 1-kb tiles, normalized to library depth, and a pseudocount of '1' was added before enrichment values over input were determined. Each ChIP-seq sample was adjusted using a correction factor based on median input levels and median background levels to reach median background enrichment of 1 to correct for unequal ChIP efficiency. Replicates were averaged for genomic 1-kb tile analyses.

ChIP-seq analysis on transposon consensus sequences: Genome mapping reads longer than 23 nucleotides were mapped to TE consensus sequences using bowtie (v.1.3.0; settings: -f -v 3 -a --best --strata --sam) allowing up to 3 mismatches. Reads mapping to multiple elements were assigned to the position with the best mapping. Reads mapping to multiple positions were randomly distributed. To obtain one value per element, library depth-normalized ChIP and input reads were averaged over all nucleotide positions of each element. ChIP-seq enrichment was calculated with a pseudo count of 1 and adjusted using sample-specific correction factors determined from background 1 kb tiles to achieve median background enrichments of 1.

Small RNA-Seq Analysis: Raw reads were trimmed for linker sequences, barcodes and the 4/6 random nucleotides before mapping to the *Drosophila melanogaster* genome (dm6), using Bowtie (version.1.3.0, settings: -f -v 3 -a --best --strata --sam) with 0 mismatches allowed. Genome mapping reads were intersected with Flybase genome annotations (r6.40) using BEDTools to allow the removal of reads mapping to rRNA, tRNA, snRNA, snoRNA loci and the mitochondrial genome. For TE mappings, all genome mappers were used allowing no mismatches. Reads mapping to multiple elements were assigned to the best match. Reads mapping equally well to multiple positions were randomly distributed. Libraries were normalized to 1 million sequenced microRNA reads. For calculation of piRNAs mapping to TEs, only antisense piRNAs were considered, and counts were normalized to TE length. For classification of tiles and transposons into Rhino-independent and Rhino-dependent TEs in ovaries and testes, a binary cutoff of at a 2-fold reduction in antisense piRNA levels in *rhino* knockdown compared to control was applied based on the control samples of the respective tissue.

Local unique piRNA cluster mapping piRNAs: piRNA counts of major piRNA clusters relevant in ovaries or testes were determined using cluster definitions established by Chen et al. (Chen and Aravin,

2023). Locus-unique multi-mappers were obtained by intersecting the 5′ ends of the genome aligned reads with the cluster coordinates. Only reads intersecting only with a single source locus and nowhere else in the genome were allowed. Reads mapping multiple times within one source locus were allowed but only counted once. To account for genotype differences, tiles with a read count of zero in any of the analyzed genotypes were excluded from the analysis.

REFERENCES

AASLAND, R. & STEWART, A. 1995. The chromo shadow domain, a second chromo domain in heterochromatin-binding protein 1, HP1. *Nucleic Acids Res,* 23**,** 3163-73.

ALLSHIRE, R. C. & MADHANI, H. D. 2018. Ten principles of heterochromatin formation and function. *Nat Rev Mol Cell Biol,* 19**,** 229-244.

ALTSCHUL, S. F., MADDEN, T. L., SCHAFFER, A. A., ZHANG, J., ZHANG, Z., MILLER, W. & LIPMAN, D. J. 1997. Gapped BLAST and PSI-BLAST: a new generation of protein database search programs. *Nucleic Acids Res,* 25**,** 3389-402.

ANDERSEN, P. R., TIRIAN, L., VUNJAK, M. & BRENNECKE, J. 2017. A heterochromatin-dependent transcription machinery drives piRNA expression. *Nature,* 549**,** 54-59.

BANNISTER, A. J., ZEGERMAN, P., PARTRIDGE, J. F., MISKA, E. A., THOMAS, J. O., ALLSHIRE, R. C. & KOUZARIDES, T. 2001. Selective recognition of methylated lysine 9 on histone H3 by the HP1 chromo domain. *Nature,* 410**,** 120-4.

BAUMGARTNER, L., HANDLER, D., PLATZER, S. W., YU, C., DUCHEK, P. & BRENNECKE, J. 2022. The Drosophila ZAD zinc finger protein Kipferl guides Rhino to piRNA clusters. *Elife,* 11.

BOURQUE, G., BURNS, K. H., GEHRING, M., GORBUNOVA, V., SELUANOV, A., HAMMELL, M., IMBEAULT, M., IZSVAK, Z., LEVIN, H. L., MACFARLAN, T. S., MAGER, D. L. & FESCHOTTE, C. 2018. Ten things you should know about transposable elements. *Genome Biol,* 19**,** 199.

BRANDT, B. W., FEENSTRA, K. A. & HERINGA, J. 2010. Multi-Harmony: detecting functional specificity from sequence alignment. *Nucleic Acids Res,* 38**,** W35-40.

BRASHER, S. V., SMITH, B. O., FOGH, R. H., NIETLISPACH, D., THIRU, A., NIELSEN, P. R., BROADHURST, R. W., BALL, L. J., MURZINA, N. V. & LAUE, E. D. 2000. The structure of mouse HP1 suggests a unique mode of single peptide recognition by the shadow chromo domain dimer. *EMBO J,* 19**,** 1587-97.

BRENNECKE, J., ARAVIN, A. A., STARK, A., DUS, M., KELLIS, M., SACHIDANANDAM, R. & HANNON, G. J. 2007. Discrete Small RNA-Generating Loci as Master Regulators of Transposon Activity in Drosophila. *Cell,* 128**,** 1089-103.

CHEN, P. & ARAVIN, A. A. 2023. Genetic control of a sex-specific piRNA program. *Curr Biol,* 33**,** 1825-1835 e3.

CHEN, P., LUO, Y. & ARAVIN, A. A. 2021. RDC complex executes a dynamic piRNA program during Drosophila spermatogenesis to safeguard male fertility. *PLoS Genet,* 17**,** e1009591.

CHEN, Y. A., STUWE, E., LUO, Y., NINOVA, M., LE THOMAS, A., ROZHAVSKAYA, E., LI, S., VEMPATI, S., LAVER, J. D., PATEL, D. J., SMIBERT, C. A., LIPSHITZ, H. D., TOTH, K. F. & ARAVIN, A. A. 2016. Cutoff Suppresses RNA Polymerase II Termination to Ensure Expression of piRNA Precursors. *Mol Cell,* 63**,** 97-109.

COORDINATORS, N. R. 2018. Database resources of the National Center for Biotechnology Information. *Nucleic Acids Res,* 46**,** D8-D13.

CZECH, B., MUNAFO, M., CIABRELLI, F., EASTWOOD, E. L., FABRY, M. H., KNEUSS, E. & HANNON, G. J. 2018. piRNA-Guided Genome Defense: From Biogenesis to Silencing. *Annu Rev Genet,* 52**,** 131-157.

EISSENBERG, J., JAMES, T., FOSTER-HARTNETT, D., HARTNETT, T., NGAN, V. & ELGIN, S. 1990. Mutation in a heterochromatin-specific chromosomal protein is associated with suppression of position-effect variegation in Drosophila melanogaster. *Proc Natl Acad Sci U S A,* 87**,** 9923-7.

EISSENBERG, J., MORRIS, G., REUTER, G. & HARTNETT, T. 1992. The heterochromatin-associated protein HP-1 is an essential protein in Drosophila with dosage-dependent effects on position-effect variegation. *Genetics,* 131**,** 345-52.

ELMAGHRABY, M. F., ANDERSEN, P. R., PUHRINGER, F., HOHMANN, U., MEIXNER, K., LENDL, T., TIRIAN, L. & BRENNECKE, J. 2019. A Heterochromatin-Specific RNA Export Pathway Facilitates piRNA Production. *Cell,* 178**,** 964-979 e20.

EVANS, R., O'NEILL, M., PRITZEL, A., ANTROPOVA, N., SENIOR, A., GREEN, T., ŽÍDEK, A., BATES, R., BLACKWELL, S., YIM, J., RONNEBERGER, O., BODENSTEIN, S., ZIELINSKI, M., BRIDGLAND, A., POTAPENKO, A., COWIE, A., TUNYASUVUNAKOOL, K., JAIN, R., CLANCY, E., KOHLI, P., JUMPER, J. & HASSABIS, D. 2022. Protein complex prediction with AlphaFold-Multimer. *bioRxiv***,** 2021.10.04.463034.

FEDOROFF, N. V. 2012. Presidential address. Transposable elements, epigenetics, and genome evolution. *Science,* 338**,** 758-67.

GASPAR, I., WIPPICH, F. & EPHRUSSI, A. 2017. Enzymatic production of single-molecule FISH and RNA capture probes. *RNA,* 23**,** 1582-1591.

GOKCEZADE, J., SIENSKI, G. & DUCHEK, P. 2014. Efficient CRISPR/Cas9 Plasmids for Rapid and Versatile Genome Editing in Drosophila. *G3 (Bethesda)*.

GRENTZINGER, T., OBERLIN, S., SCHOTT, G., HANDLER, D., SVOZIL, J., BARRAGAN-BORRERO, V., HUMBERT, A., DUHARCOURT, S., BRENNECKE, J. & VOINNET, O. 2020. A universal method for the rapid isolation of all known classes of functional silencing small RNAs. *Nucleic Acids Res,* 48**,** e79.

HOANG, D. T., CHERNOMOR, O., VON HAESELER, A., MINH, B. Q. & VINH, L. S. 2018. UFBoot2: Improving the Ultrafast Bootstrap Approximation. *Mol Biol Evol,* 35**,** 518-522.

JACOBS, S. A., TAVERNA, S. D., ZHANG, Y., BRIGGS, S. D., LI, J., EISSENBERG, J. C., ALLIS, C. D. & KHORASANIZADEH, S. 2001. Specificity of the HP1 chromo domain for the methylated N-terminus of histone H3. *EMBO J,* 20**,** 5232-41.

JAMES, T. C. & ELGIN, S. C. 1986. Identification of a nonhistone chromosomal protein associated with heterochromatin in Drosophila melanogaster and its gene. *Mol Cell Biol,* 6**,** 3862-72.

JUMPER, J., EVANS, R., PRITZEL, A., GREEN, T., FIGURNOV, M., RONNEBERGER, O., TUNYASUVUNAKOOL, K., BATES, R., ZIDEK, A., POTAPENKO, A., BRIDGLAND, A., MEYER, C., KOHL, S. A. A., BALLARD, A. J., COWIE, A., ROMERA-PAREDES, B., NIKOLOV, S., JAIN, R., ADLER, J., BACK, T., PETERSEN, S., REIMAN, D., CLANCY, E., ZIELINSKI, M., STEINEGGER, M., PACHOLSKA, M., BERGHAMMER, T., BODENSTEIN, S., SILVER, D., VINYALS, O., SENIOR, A. W., KAVUKCUOGLU, K., KOHLI, P. & HASSABIS, D. 2021. Highly accurate protein structure prediction with AlphaFold. *Nature,* 596**,** 583-589.

KALYAANAMOORTHY, S., MINH, B. Q., WONG, T. K. F., VON HAESELER, A. & JERMIIN, L. S. 2017. ModelFinder: fast model selection for accurate phylogenetic estimates. *Nat Methods,* 14**,** 587-589.

KATOH, K. & TOH, H. 2008. Recent developments in the MAFFT multiple sequence alignment program. *Brief Bioinform,* 9**,** 286-98.

KELLER, C., ADAIXO, R., STUNNENBERG, R., WOOLCOCK, K. J., HILLER, S. & BUHLER, M. 2012. HP1(Swi6) mediates the recognition and destruction of heterochromatic RNA transcripts. *Mol Cell,* 47**,** 215-27.

KLATTENHOFF, C., XI, H., LI, C., LEE, S., XU, J., KHURANA, J. S., ZHANG, F., SCHULTZ, N., KOPPETSCH, B. S., NOWOSIELSKA, A., SEITZ, H., ZAMORE, P. D., WENG, Z. & THEURKAUF, W. E. 2009. The Drosophila HP1 homolog Rhino is required for transposon silencing and piRNA production by dual-strand clusters. *Cell,* 138**,** 1137-49.

KNEUSS, E., MUNAFO, M., EASTWOOD, E. L., DEUMER, U. S., PREALL, J. B., HANNON, G. J. & CZECH, B. 2019. Specialization of the Drosophila nuclear export family protein Nxf3 for piRNA precursor export. *Genes Dev,* 33**,** 1208-1220.

LACHNER, M., O'CARROLL, D., REA, S., MECHTLER, K. & JENUWEIN, T. 2001. Methylation of histone H3 lysine 9 creates a binding site for HP1 proteins. *Nature,* 410**,** 116-20.

LE THOMAS, A., STUWE, E., LI, S., DU, J., MARINOV, G., ROZHKOV, N., CHEN, Y. C., LUO, Y., SACHIDANANDAM, R., TOTH, K. F., PATEL, D. & ARAVIN, A. A. 2014. Transgenerationally inherited piRNAs trigger piRNA biogenesis by changing the chromatin of piRNA clusters and inducing precursor processing. *Genes Dev,* 28**,** 1667-80.

LEE, D. H., RYU, H. W., KIM, G. W. & KWON, S. H. 2019. Comparison of three heterochromatin protein 1 homologs in Drosophila. *J Cell Sci,* 132.

LEE, T. I., JOHNSTONE, S. E. & YOUNG, R. A. 2006. Chromatin immunoprecipitation and microarray-based analysis of protein location. *Nat Protoc,* 1**,** 729-48.

LETUNIC, I. & BORK, P. 2021. Interactive Tree Of Life (iTOL) v5: an online tool for phylogenetic tree display and annotation. *Nucleic Acids Res,* 49**,** W293-W296.

LEVIN, H. L. & MORAN, J. V. 2011. Dynamic interactions between transposable elements and their hosts. *Nat Rev Genet,* 12**,** 615-27.

LEVINE, M. T., MCCOY, C., VERMAAK, D., LEE, Y. C., HIATT, M. A., MATSEN, F. A. & MALIK, H. S. 2012. Phylogenomic analysis reveals dynamic evolutionary history of the Drosophila heterochromatin protein 1 (HP1) gene family. *PLoS Genet,* 8**,** e1002729.

MILES, A. J., RAMALLI, S. G. & WALLACE, B. A. 2022. DichroWeb, a website for calculating protein secondary structure from circular dichroism spectroscopic data. *Protein Sci,* 31**,** 37-46.

MINH, B. Q., SCHMIDT, H. A., CHERNOMOR, O., SCHREMPF, D., WOODHAMS, M. D., VON HAESELER, A. & LANFEAR, R. 2020. IQ-TREE 2: New Models and Efficient Methods for Phylogenetic Inference in the Genomic Era. *Mol Biol Evol,* 37**,** 1530-1534.

MIRDITA, M., SCHUTZE, K., MORIWAKI, Y., HEO, L., OVCHINNIKOV, S. & STEINEGGER, M. 2022. ColabFold: making protein folding accessible to all. *Nat Methods,* 19**,** 679-682.

MOHN, F., SIENSKI, G., HANDLER, D. & BRENNECKE, J. 2014. The rhino-deadlock-cutoff complex licenses noncanonical transcription of dual-strand piRNA clusters in Drosophila. *Cell,* 157**,** 1364-79.

OZATA, D. M., GAINETDINOV, I., ZOCH, A., O'CARROLL, D. & ZAMORE, P. D. 2018. PIWI-interacting RNAs: small RNAs with big functions. *Nat Rev Genet*.

PETTERSEN, E. F., GODDARD, T. D., HUANG, C. C., MENG, E. C., COUCH, G. S., CROLL, T. I., MORRIS, J. H. & FERRIN, T. E. 2021. UCSF ChimeraX: Structure visualization for researchers, educators, and developers. *Protein Sci,* 30**,** 70-82.

PROVENCHER, S. W. & GLOCKNER, J. 1981. Estimation of globular protein secondary structure from circular dichroism. *Biochemistry,* 20**,** 33-7.

SCHINDELIN, J., ARGANDA-CARRERAS, I., FRISE, E., KAYNIG, V., LONGAIR, M., PIETZSCH, T., PREIBISCH, S., RUEDEN, C., SAALFELD, S., SCHMID, B., TINEVEZ, J. Y., WHITE, D. J., HARTENSTEIN, V., ELICEIRI, K., TOMANCAK, P. & CARDONA, A. 2012. Fiji: an open-source platform for biological-image analysis. *Nat Methods,* 9**,** 676-82.

SMOTHERS, J. F. & HENIKOFF, S. 2000. The HP1 chromo shadow domain binds a consensus peptide pentamer. *Curr Biol,* 10**,** 27-30.

STEINEGGER, M. & SODING, J. 2017. MMseqs2 enables sensitive protein sequence searching for the analysis of massive data sets. *Nat Biotechnol,* 35**,** 1026-1028.

UNIPROT, C. 2021. UniProt: the universal protein knowledgebase in 2021. *Nucleic Acids Res,* 49**,** D480-D489.

VERMAAK, D., HENIKOFF, S. & MALIK, H. S. 2005. Positive selection drives the evolution of rhino, a member of the heterochromatin protein 1 family in Drosophila. *PLoS Genet,* 1**,** 96-108.

VERMAAK, D. & MALIK, H. S. 2009. Multiple roles for heterochromatin protein 1 genes in Drosophila. *Annu Rev Genet,* 43**,** 467-92.

WATERHOUSE, A. M., PROCTER, J. B., MARTIN, D. M., CLAMP, M. & BARTON, G. J. 2009. Jalview Version 2--a multiple sequence alignment editor and analysis workbench. *Bioinformatics,* 25**,** 1189-91.

WEI, X., EICKBUSH, D. G., SPEECE, I. & LARRACUENTE, A. M. 2021. Heterochromatin-dependent transcription of satellite DNAs in the Drosophila melanogaster female germline. *Elife,* 10.

YU, B., CASSANI, M., WANG, M., LIU, M., MA, J., LI, G., ZHANG, Z. & HUANG, Y. 2015. Structural insights into Rhino-mediated germline piRNA cluster formation. *Cell Res,* 25**,** 525-8.

ZHANG, Z., WANG, J., SCHULTZ, N., ZHANG, F., PARHAD, S. S., TU, S., VREVEN, T., ZAMORE, P. D., WENG, Z. & THEURKAUF, W. E. 2014. The HP1 homolog rhino anchors a nuclear complex that suppresses piRNA precursor splicing. *Cell,* 157**,** 1353-63.

654 **Figure 1, Figure Supplement 1**

655 Multiple sequence alignment of HP1 family proteins across *Drosophila* species. Further details on
656 protein accessions and identifiers are documented in Supplementary File 1. Multi-Relief representation
657 indicates residues that differ significantly in Rhino homologs versus other HP1 variant proteins.

658

659 **Figure 1, Figure Supplement 2**

660 Phylogenetic tree illustrating the evolutionary relationship of zinc finger associated domain (ZAD)-
661 containing zinc finger proteins based on ZAD protein sequence. Blue labels indicate *Drosophila*
662 *melanogaster* proteins, red labels mark Kipferl orthologs in different species. Branches that are supported
663 by an ultrafast bootstrap (UFBoot) value >=95% are indicated by a black dot. Branch lengths represent
664 the inferred number of amino acid substitutions per site, and branch labels are composed of gene name
665 (if available), genus, species, and accession number.

666

667 **Figure 1, Figure Supplement 3**

668 Diagnostic plots for rank 1-5 for the AlphaFold2 Multimer prediction of the Rhino chromodomain with
669 the Kipferl ZnF cluster 1. **(A)** PAE plot **(B)** pLDDT plot **(C)** Superposition on the Rhino chromodomain
670 of the models for rank 1 – 5, as Cα trace.

671

672 **Figure 2, Figure Supplement 1**

673 Individual line graphs depicting SEC-MALS results for the examined Rhino chromodomain constructs
674 with in solution molecular weight measurements depicted in red. **(B)** Bar graph summarizing circular
675 dichroism spectrum measurements for the tested Rhino chromodomain constructs.

676
677
678
679
680
681
682
683
684
685
686
687

Figure 1
figure supplement 1

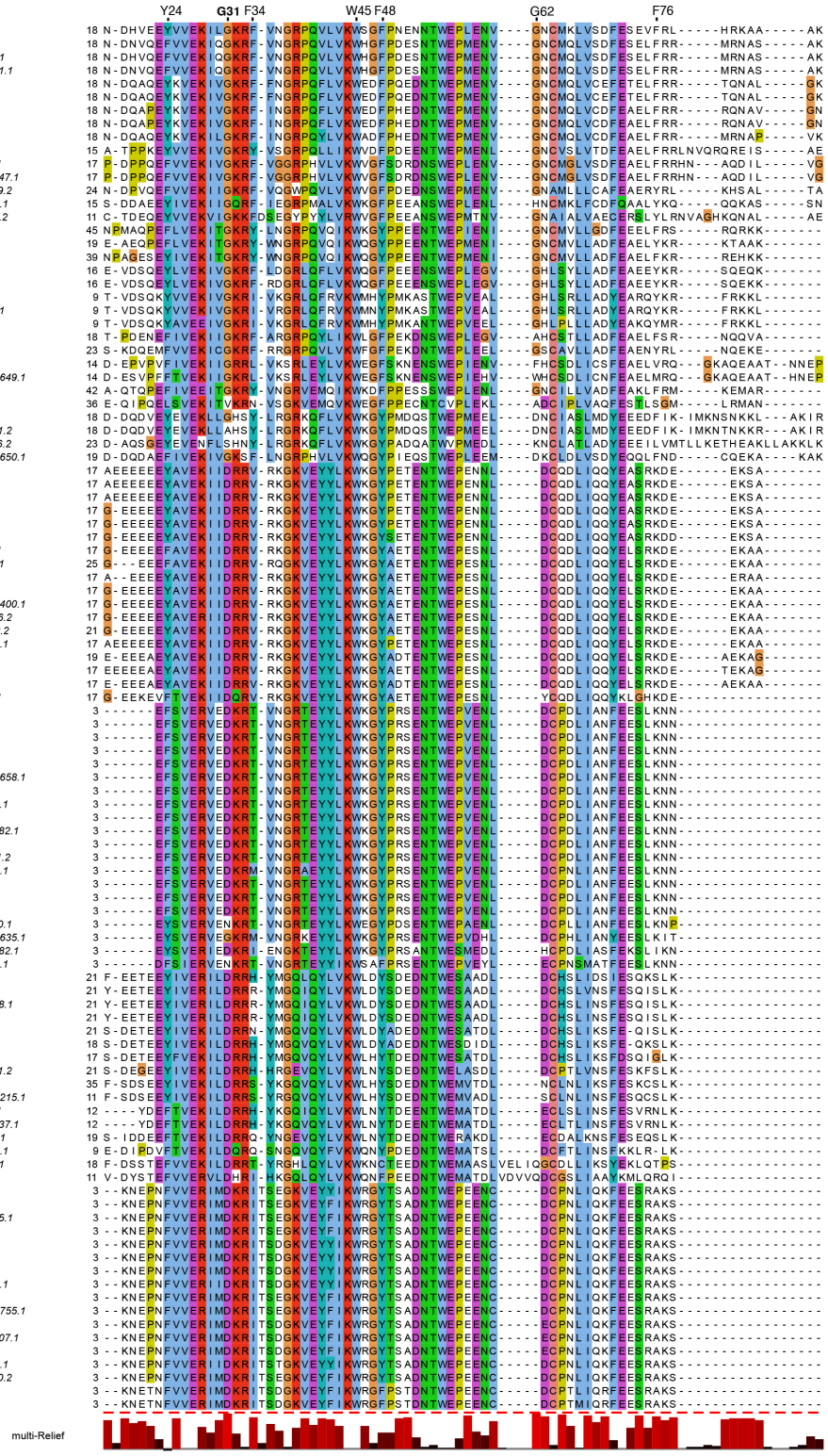

Figure 1
figure supplement 2

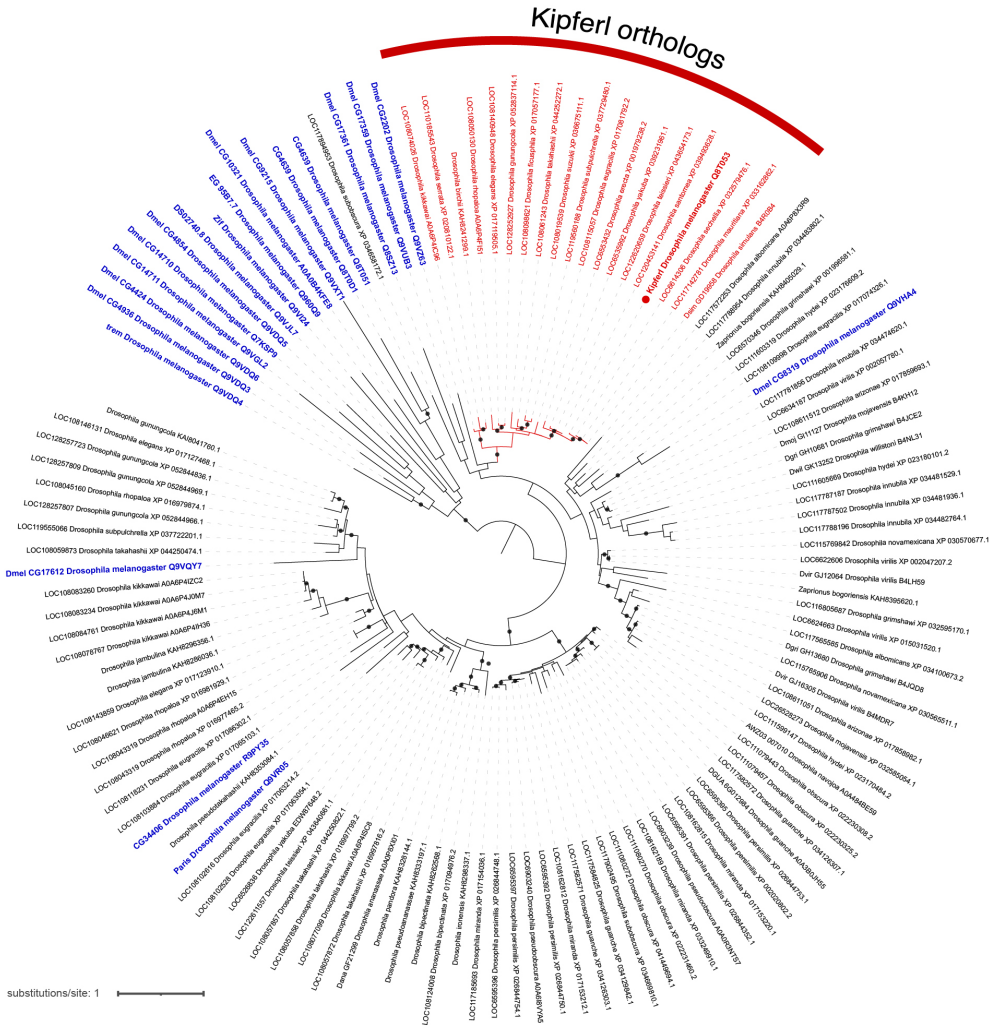

Figure 1
figure supplement 3

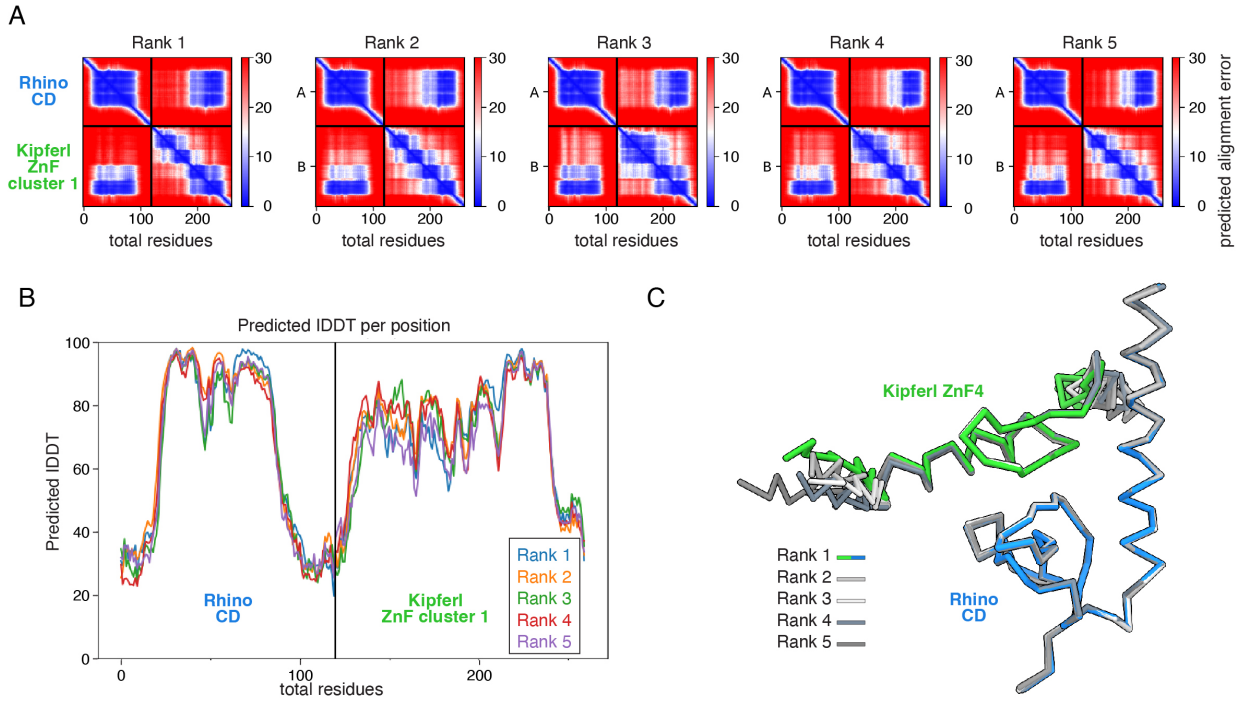

690
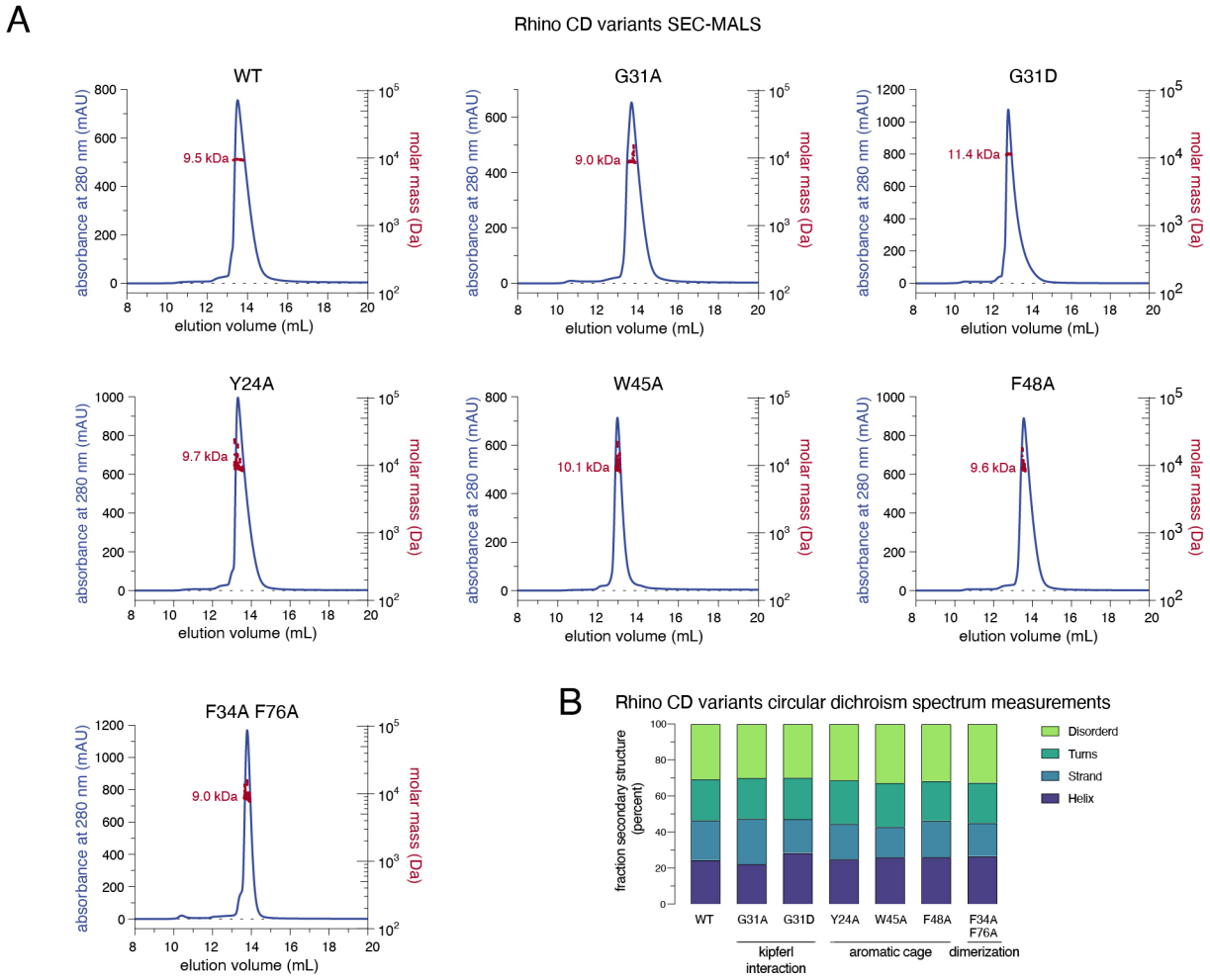
Figure 2
figure supplement 1